

Plasma sheath studies using a physical treatment of electron emission from a dielectric wall

K. Bradshaw,¹ P. Cagas,¹ A. Hakim,² and B. Srinivasan^{1, a)}

¹⁾*Kevin T. Crofton Department of Aerospace and Ocean Engineering, Virginia Tech, Blacksburg, Virginia 24061, USA*

²⁾*Princeton Plasma Physics Laboratory, Princeton, New Jersey 08543-0451, USA*

(Dated: 26 October 2022)

When a plasma sheath forms next to a dielectric wall, material properties determine electron absorption and reflection from the surface, impacting the sheath formation and structure. This interaction may be modeled from quantum mechanical first principles, and has important applications to plasma thrusters and fusion devices. In this work, electron reflection from the wall is implemented as a boundary condition in a continuum kinetic framework and the sheath is simulated for multiple dielectric materials. The results presented here demonstrate that the material parameters have significant effect on the resulting sheath profile and particle distribution functions. Surfaces with high reflection rates see the formation of a space-charge limited sheath where the potential is positive relative to the wall.

I. INTRODUCTION

As plasma interacts with an absorbing surface, the electrons have a higher mobility and impact the boundary at a quicker rate than the less mobile ions. The result of this is a barrier field allowing the wall to float at a negative potential, accelerating ions and retarding electrons. This positive space-charge region where the potential profile drops towards the wall is called the plasma sheath.¹⁻³ The sheath entrance is typically defined by the point where the Bohm sheath criterion is met;⁴ that is, where the ion velocity exceeds the Bohm speed

$$u_B = \sqrt{\frac{ZT_e}{m_i}}. \quad (1)$$

In this equation Z is the ionization state, T_e the electron temperature, and m_i the electron mass. It should be noted that this model is simplified, as it has been shown the sheath entrance cannot rigorously be defined as a single point.^{5,6} However, it is sufficient for the purposes of this work to think of the sheath entrance as occurring several Debye lengths λ_D from the wall, where

$$\lambda_D = \sqrt{\frac{\epsilon_0 T_e}{n_e q_e^2}}, \quad (2)$$

with ϵ_0 being the permittivity of free space, n_e the electron density, and q_e the electron charge. This work builds on a previous examination of the classical plasma sheath using continuum kinetic simulations.⁷

The surface interacting with the plasma will cause some electrons to be emitted back into the sheath instead of acting as a perfectly absorbing boundary. This emission is characterized by the electron flux gain γ , defined as the ratio of inward flux to outward flux at the wall. For lower values of $\gamma < 1$, the sheath which forms is classical; that is, monotonic, with a negative wall potential relative to the plasma edge. At some

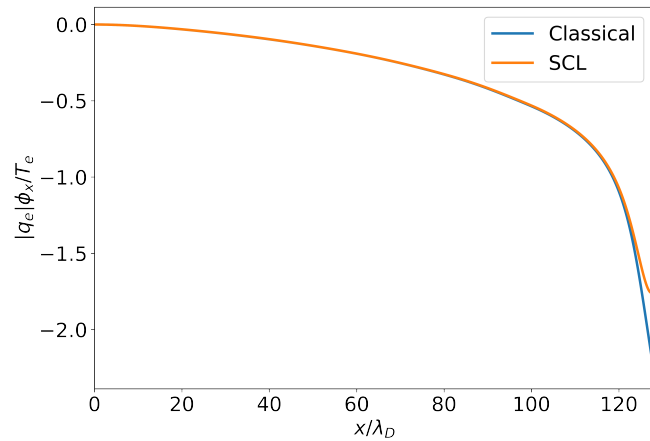


FIG. 1. Sheath potential profiles for the classical sheath ($\gamma < \gamma_c$) and SCL sheath ($\gamma > \gamma_c$) solutions.

critical gain γ_c , a non-monotonic space-charge limited (SCL) sheath forms for $\gamma_c < \gamma < 1$. The potential profiles of the classical and SCL solutions are displayed in Fig. 1. Finally, while less relevant for this work, for $\gamma \geq 1$ it has been shown that the sheath will transition to an inverse sheath where the wall potential is positive relative to the plasma edge.^{8,9}

Numerous papers have examined the effect of strong electron emission on the sheath, however, previous works have typically treated the emitted electron population as a cold Maxwellian injection typical of thermionic probe emission.^{9,10} In the case of emission from a material under electron impact, the relationship between the electron flux into the wall and the emitted population is more complicated.¹¹ The work presented here shows the effects of implementing a physical treatment of emission as a boundary condition for simulations of the plasma sheath formed by interaction with a dielectric wall.

A number of approaches have been taken to model the emitted electron population. Furman and Pivi in their approach to the problem model the three populations of emitted electrons separately.¹² These are the true secondary electrons which are emitted directly from the material, rediffused electrons which

^{a)}srinbhu@vt.edu

enter the material and are eventually reemitted, and the reflected electrons which fail to penetrate the material. At low energies, the reflected population dominates the other two and is the focus of this work. While Furman and Pivi's empirical treatment of the electron emission fits well to electron beam data at higher energies, the quantum mechanical derivation of the reflection function for dielectric materials by Bronold and Fehske¹³ is preferred for this work due to its first principles approach to lower energy plasma material interaction. While both the backscattering and rediffusion of particles are considered by Bronold and Fehske, as the rediffusion term is both less physically significant and more computationally expensive to implement than reflection, it is not considered within the scope of this paper.

II. NUMERICAL MODEL AND PROBLEM SETUP

A. Numerical model

Kinetic theory of plasmas describes the evolution of the distribution functions for the particle species through the Vlasov-Maxwell system of equations. The core of this system is the Boltzmann equation

$$\frac{\partial f_s}{\partial t} + \mathbf{v} \cdot \frac{\partial f_s}{\partial \mathbf{x}} + \frac{q}{m} (\mathbf{E} + \mathbf{v} \times \mathbf{B}) \cdot \frac{\partial f_s}{\partial \mathbf{v}} = S_{src,s} + S_{coll,s}, \quad (3)$$

which describes the behavior of the distribution in time, with Maxwell's equations evolving the electromagnetic fields. Here, $f_s(\mathbf{x}, \mathbf{v}, t)$ is the particle distribution function for species s , $S_{src,s}$ is a source injection term, and $S_{coll,s}$ is a collision term.

The collision term is modeled by a Lenard-Bernstein¹⁴ (LBO, known also as a Dougherty operator) collision operator. This operator takes the form

$$S_{coll,s} = \sum_r v_{sr} \frac{\partial}{\partial \mathbf{v}} \cdot \left[(\mathbf{v} - \mathbf{u}_{sr}) f_s + v_{tsr}^2 \frac{\partial f_s}{\partial \mathbf{v}} \right], \quad (4)$$

where there is a summation over each species r being collided with. These terms are dependent on the primitive moments \mathbf{u}_{sr} and v_{tsr} , representing the cross flow velocity and thermal speed, respectively.

The discontinuous Galerkin¹⁵ (DG) method yields the full discretized Vlasov-Maxwell-Fokker-Planck (VM-FP) system of equations¹⁶⁻¹⁹, which is evolved in time using a strong-stability preserving Runge-Kutta scheme.

The Bronold and Fehske electron backscattering model expresses the probability that an electron will penetrate a material as a function of incoming energy E' and angle cosine μ'

$$\mathcal{T}(E', \mu') = \frac{4\bar{m}_e k p}{(\bar{m}_e k + p)^2}. \quad (5)$$

Here χ and \bar{m}_e are the electron affinity and effective conduction band electron mass ratio, respectively, and $k = \sqrt{E' - \chi} \mu'$ and $p = \sqrt{\bar{m}_e E'} \eta$ are the z -components of the electron momentum outside and inside the material with η

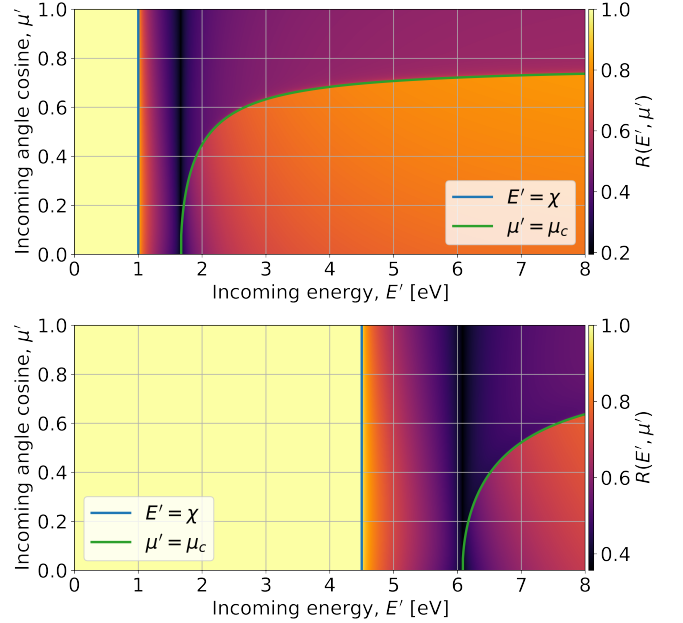


FIG. 2. Reflection function for magnesium oxide (top, reproduced from Cagas, P., 2018, Continuum Kinetic Simulations of Plasma Sheaths and Instabilities (Doctoral dissertation, Virginia Tech), with the permission of Petr Cagas), and boron nitride (bottom). Below the $E' = \chi$ threshold, all particles are perfectly reflected from the material. Due to the higher material χ , this region is much larger for the boron nitride resulting in a higher γ .

being the angle cosine associated with the latter. η can be related to μ' by the equation

$$\eta = \sqrt{1 - (1 - \mu'^2) \frac{E' - \chi}{\bar{m}_e E'}}. \quad (6)$$

To account for imperfections in the material, this equation is modified, with a fitting factor C representing the wall roughness, to

$$\mathcal{T}(E', \mu') = \frac{\mathcal{T}(E', \mu')}{1 + C/\mu'} + \frac{C/\mu'}{1 + C\mu'} \int_{\mu_c}^1 d\mu'' \mathcal{T}(E', \mu''). \quad (7)$$

For this work, a value of $C = 2$ is used. As Eq. 7 gives the sticking probability, the electron reflection probability is

$$R(E', \mu') = 1 - \mathcal{T}(E', \mu'), \quad (8)$$

which can be discretized as a boundary condition²⁰ to yield:

$$\mathcal{R}_{X,kl}^g = \int_{I_p} R^g(E^g(\eta_v), \mu^g(\eta_v)) \hat{\psi}_l(-\eta_x, \eta_y, \eta_z, -\eta_{v_x}, \eta_{v_y}, \eta_{v_z}) \hat{\psi}_k(\eta_x, \eta_v) d\eta_x d\eta_v. \quad (9)$$

This is plotted for a low electron affinity case and high electron affinity case in Fig. 2. The materials chosen to represent these cases are magnesium oxide ($\chi = 1.0$ eV, $\bar{m}_e = 0.4$)¹³ and boron nitride ($\chi = 4.5$ eV,²¹ $\bar{m}_e = 0.26$)²², respectively. Note that for $E' < \chi$ perfect reflection occurs.

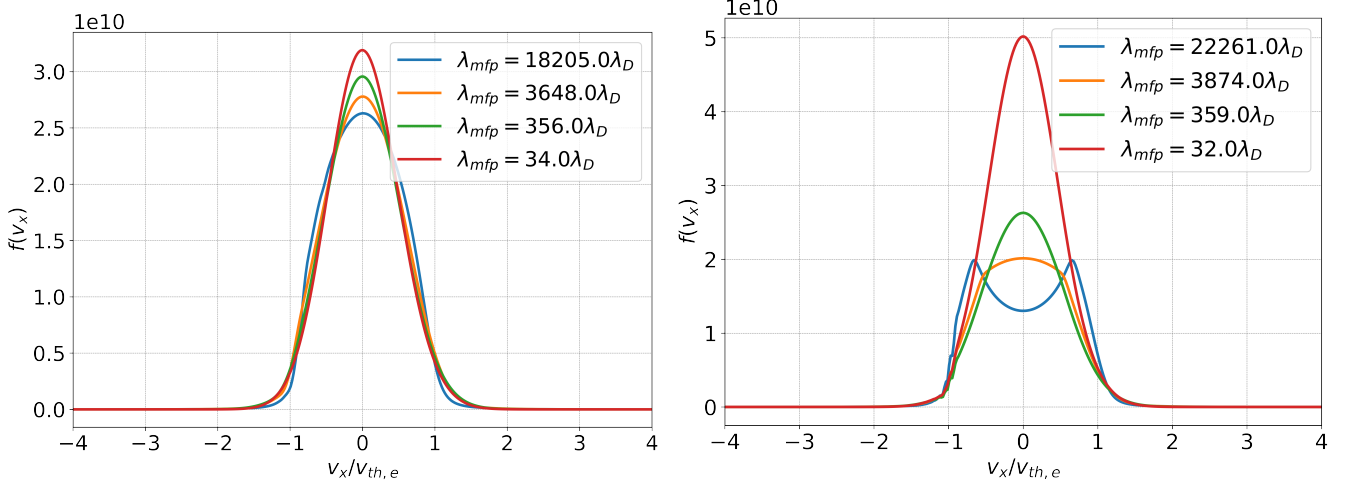


FIG. 3. Comparison of 1X1V electron distribution at the sheath entrance (left) and material surface (right) for different choices of mean free path. Note that the mean free path is affected by the cooling of the plasma over time. If collisions are too low in the presheath, the incoming plasma at the sheath entrance is not fully thermalized and a cutoff exists. If collisions are too high near the wall, the shift in the distribution function and overall sheath behavior due to emission is damped out before it can evolve.

B. Problem setup

The full VM-FP system of equations is 6D in space and velocity (3X3V). However, for the purposes of the simulations here, 1X2V dimensions are deemed sufficient to capture the behavior parallel and perpendicular to the material boundary. Two velocity space dimensions are necessary as a single velocity dimension effectively fixes $\mu' = 1$, which only permits electron motion normal to the wall. Thus, only the energy dependence is truly accounted for by the boundary condition in 1X1V. In order to properly examine the angular dependent behavior of the electron emission, an additional velocity dimension is required.

The results presented here are run on a nonuniform grid with a resolution of $N_x = N_{vx} = N_{vy} = 32$. The plasma is initialized as a Maxwellian matching the system of equations approximating a steady-state sheath profile³, with an electron and ion temperature in the presheath of $T_e = 5\text{ eV}$ and $T_i = 0.5\text{ eV}$, and density $n_e = n_i = 10^{17}\text{ m}^{-3}$. Here, thermal velocity $v_{th} = \sqrt{T_e/m}$ is used to normalize the electron results and the Bohm speed u_B is used for the ion results.

The left boundary uses a perfect reflection boundary condition to reduce the simulation domain by half for computational efficiency, while the right boundary uses the described Bronold-Fehske reflection function. The reflection function is precomputed by integrating over each velocity space cell during the initialization period of the simulation, which reduces the runtime computational cost of the reflection boundary condition.

The reflection function boundary condition was applied previously to a simple sheath simulation using the material parameters of magnesium oxide in a dissertation²³ and paper.²⁴ This work examines the dependence of the sheath formation on the material properties by comparison between two cases, a low electron affinity material (magnesium oxide) and a high

electron affinity material (boron nitride).

Since particles are being lost to the wall, the S_{src} source term for the electrons and ions is necessary to keep the total particle balance approximately constant. Initially this was implemented by taking the particle flux of each species and adding it back across a chosen source region, however, as the particle fluxes are not exactly equal this leads to a slight violation of quasineutrality in the presheath. To avoid this, it is desirable to add back equal numbers of electrons and ions with both additions being determined from the ion flux. This causes the total number of ions to remain constant, while the electrons fluctuate but approach a steady balance over time.

A standard approach to particle sources is to inject the particles at the presheath edge. This, however, invariably leads to the formation of a source sheath where a potential drop develops across the entrance of the presheath. To minimize this, the particles are added back in a Maxwellian distribution at initial temperature with the density being scaled to a linearly decreasing profile across the source region ($0 < x < 100\lambda_D$). This, as opposed to simply injecting them at the left edge, prevents the formation of a pronounced source sheath.

III. IMPACT OF COLLISIONS

The electron distribution close to the wall is non-Maxwellian, particles with a high positive velocity are absorbed while the rest are deflected by the barrier electric field. This produces a distribution with a depleted negative velocity tail, a cutoff Maxwellian which propagates to the left and encounters the pure reflection boundary condition. The result is a feedback loop where the cutoff carries over into the distribution heading back towards the wall, leading to depletion of both high energy tails of the distribution all across the domain. In order to keep the presheath in a Maxwellian distribution and

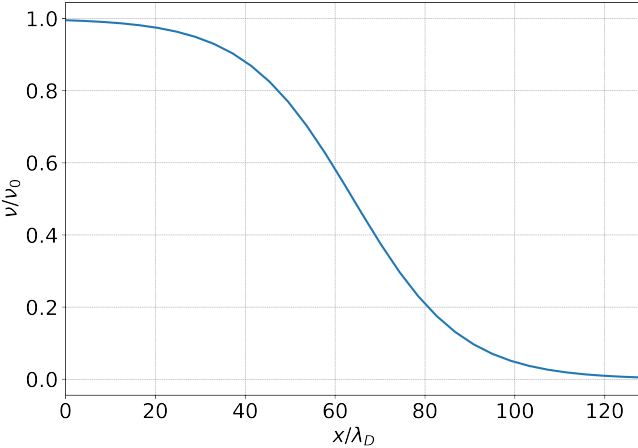


FIG. 4. Collision frequency profile across the domain. Collisions are high in the presheath so that the distribution function is fully thermalized. In the sheath, it drops to being approximately collisionless.

avoid this feedback loop, a Lenard-Bernstein¹⁴ (LBO, known also as a Dougherty operator) collision operator S_{coll} is used to smooth the distribution.¹⁹

The true physical collision frequency, due to the small size of the domain being simulated, is insufficient to fully thermalize the Maxwellian in the presheath. In a realistic scenario, the plasma will extend far enough that the mean free path of the electrons is small enough compared to the plasma length to be collisional, while being much larger than the sheath size making collisions negligible in the sheath itself. In order to model the effects of a larger plasma length on the presheath, the collision frequency must be artificially inflated. If the collisions are uniformly applied to the domain, a sufficiently high frequency to produce a smooth Maxwellian at the sheath entrance greatly alters the resulting wall distribution (Fig. 3). As the Bronold and Fehske reflection function is reliant on not just the electron flux but the particular shape of the distribution at the wall, this variation in distribution also significantly changes the overall gain behavior.

In a physical situation, collision frequency varies as $n/T^{3/2}$.²⁵ Both of these quantities drop in the sheath, though the greater weight of the temperature tends to cause collision frequency to counterintuitively rise in the sheath. However, as long as the sheath length is negligible compared to the mean free path, the sheath remains collisionless. Here, where the collision frequency is artificially inflated, this condition is not kept. Thus, while it is necessary to inflate the presheath collisionality, it is desirable to institute a spatially-varying collision profile that *decreases* as it approaches the sheath in order to fulfill the collisionless sheath condition. This is done by specifying a collision frequency profile that followed a sigmoid function and is constant in time (Fig. 4). Inter- and intra-species collisions are included for electrons and ions.

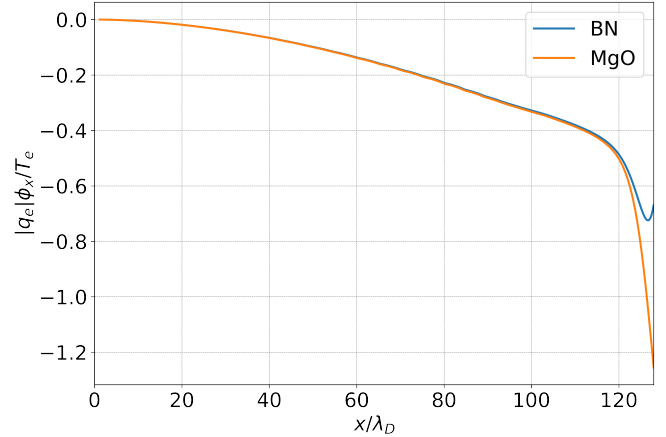


FIG. 5. Comparison of the 1X2V simulation potential profiles between boron nitride and magnesium oxide at $t\omega_{pe} = 3000$. An SCL sheath forms for the boron nitride due to the high γ , while magnesium oxide remains classical.

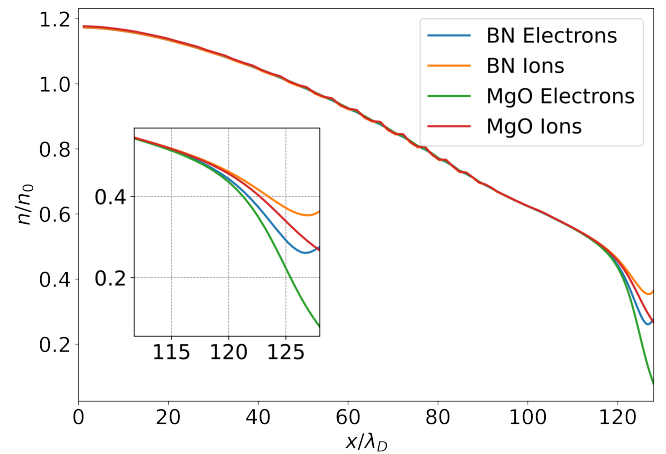


FIG. 6. Comparison of the 1X2V simulation density profiles between boron nitride and magnesium oxide at $t\omega_{pe} = 3000$. Sheath degradation and the formation of the potential barrier in the boron nitride causes accumulation of ions and electrons close to the wall.

IV. SHEATHS WITH MATERIAL BOUNDARIES RESULTS

Figure 5 plots the potential profiles for the two cases, the boron nitride develops an SCL sheath, while the magnesium oxide remains monotonic. In both cases, the emission of electrons degrades the sheath potential and the distribution function widens at the wall. Fig. 6 shows that the greater degradation in the boron nitride sheath allows an increased density at the wall as fewer particles are deflected away by the barrier field than for the magnesium oxide. The reason for these differences is made more clear by examining where the threshold at which electron energy exceeds the electron affinity of the material lies.

Fig. 7 compares the electron distribution functions of the different materials at the wall, with the electron affinity threshold marked in green. With the high affinity case, the great

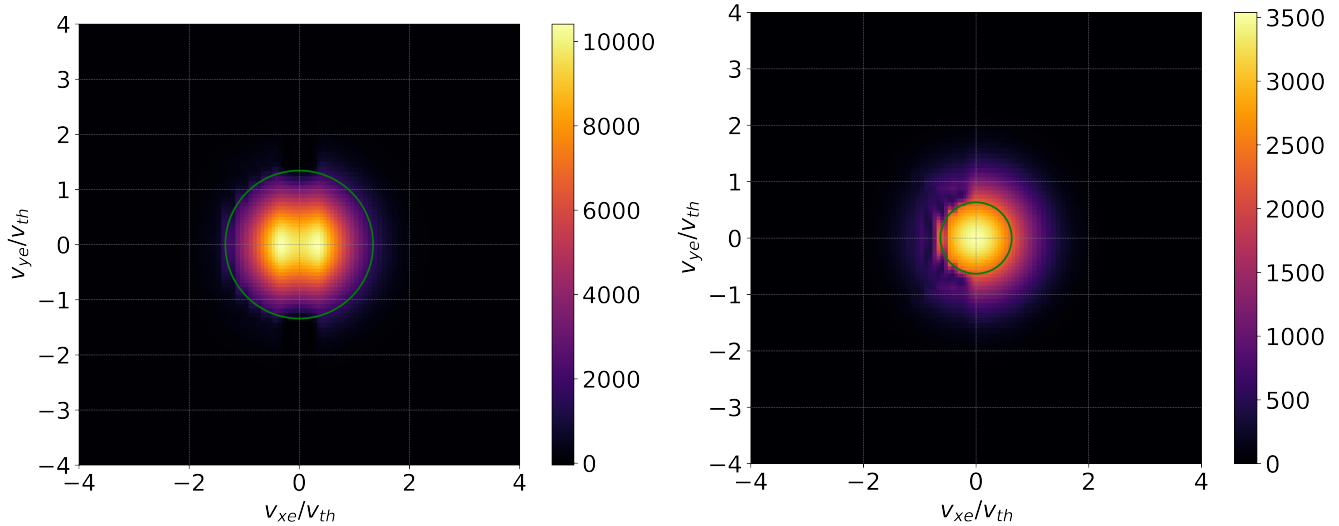


FIG. 7. Electron distribution functions at the wall for boron nitride (left) and magnesium oxide (right). The green lines represent the velocity at which energy equals the electron affinity of the respective material. Magnesium oxide remains a smooth Maxwellian entering the sheath region, while a peak forms in boron nitride due to acceleration by the potential barrier.

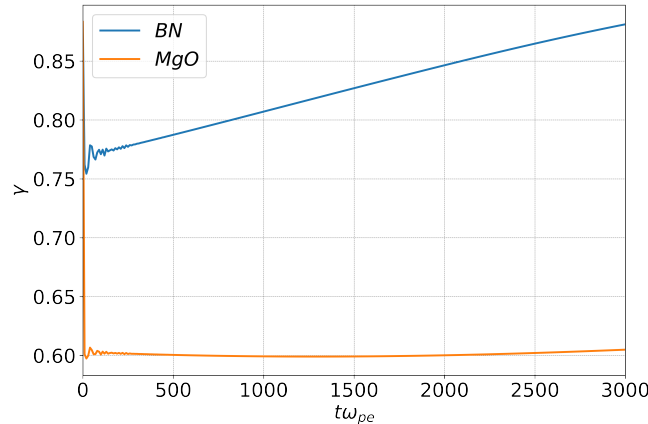


FIG. 8. γ for boron nitride surpasses the necessary γ_c to transition to an SCL sheath, while magnesium oxide remains in the classical regime.

majority of the distribution function lies inside the threshold and is reflected. Higher gain results in a greater deterioration of the sheath, which in turn changes the shape of the distribution function. For the high affinity material, the increase in potential between the minimum sheath potential and the wall potential accelerates the electrons of the distribution function, depleting the center and causing a high velocity peak to form in the v_x tail of the distribution. This does not occur in the low affinity case as the minimum sheath potential is at the wall, and the incoming distribution is a uniform Maxwellian across v_y and positive v_x velocity space. The lower electron affinity of the magnesium oxide allows the features of the reflection function to be clearly visible in the resulting distribution, with the sharp transition region at $E' = \chi$ marking a drop from pure reflection to a region of low electron population. Farther into

the higher energy portions of the distribution, the population of reflected electrons begins to increase once more.

A comparison of the gain as a function of time, shown in Fig. 8, demonstrates the higher reflection rate of the high affinity case compared to the low affinity case. The cooling of plasma with time causes the distribution function for the high affinity case to consolidate from the low-reflection region immediately outside the electron affinity to within the electron affinity threshold, causing an increase in the gain with time. This cooling also occurs in the low affinity case, but the gain does not necessarily increase as a greater portion of the distribution is present in high-reflection regions farther away from the affinity threshold, which during cooling will migrate to the low-reflection region. This results in the approximately constant gain for the low affinity case.

The difference between the electron and ion distribution functions for the two cases is presented in Fig. 9 to identify any key features. For boron nitride, the particles are not accelerated parallel to the wall by the potential, but the higher electron affinity still allows for a greater particle accumulation at the boundary than is seen in magnesium oxide. In conjunction to the acceleration of the electrons by the potential barrier, the ions in the boron nitride experience deceleration close to the wall.

The heat flux q_k of a plasma is defined as²⁶

$$q_k = \frac{1}{2} m \int (v_i - u_i)^2 (v_k - u_k) f dv, \quad (10)$$

representing the net energy transfer due to the spread of the distribution from the drift speed. Fig. 10 presents the heat flux for the two materials compared to a simple absorbing wall classical sheath. The heat flux is calculated from the total energy flux density²⁶

$$\frac{1}{2} \mathcal{Q}_{iik} = q_k + u_k(p + E) + u_i \pi_{ik}, \quad (11)$$

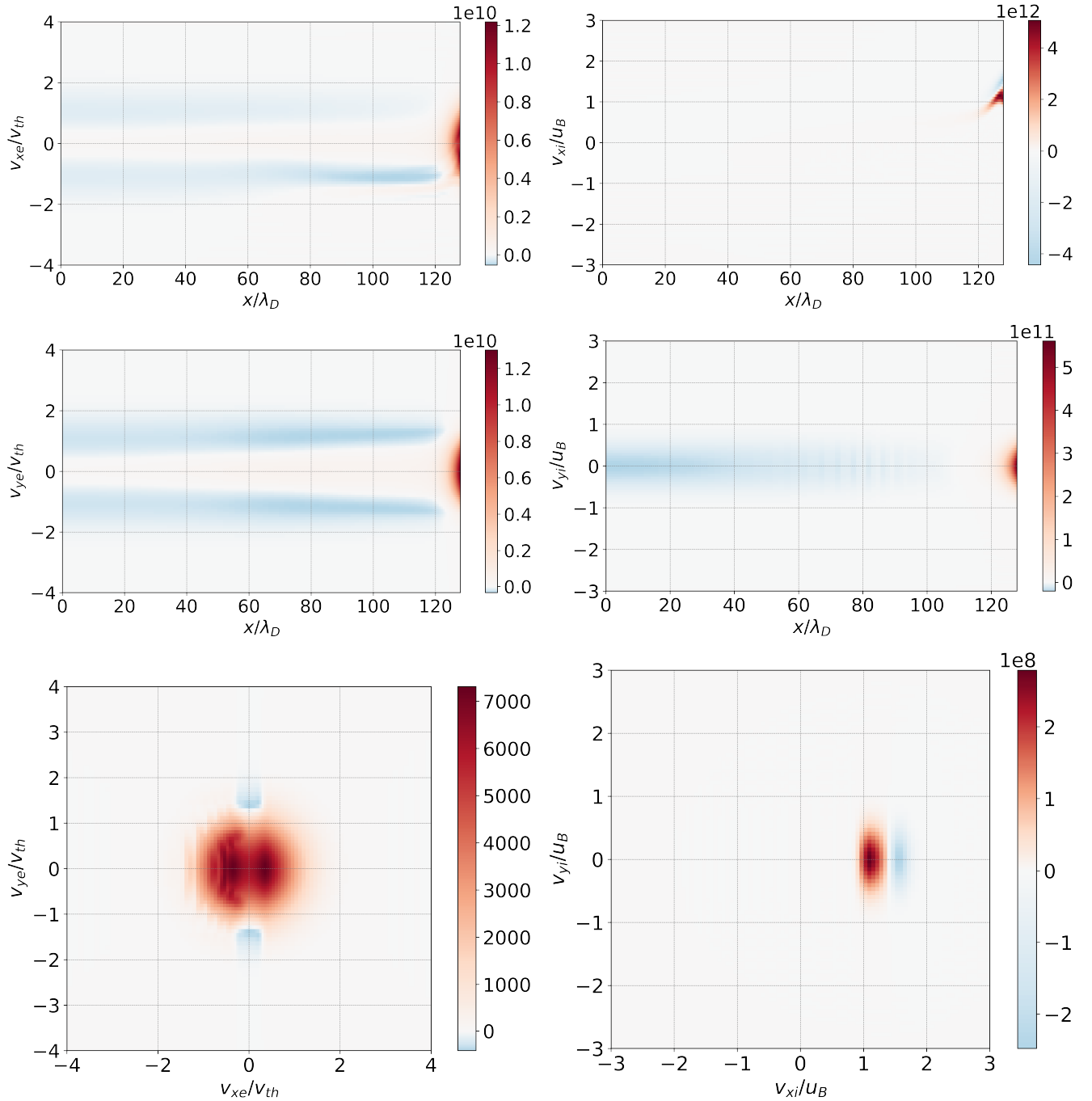


FIG. 9. Difference between electron (left) and ion (right) distribution functions of boron nitride and magnesium oxide $f_{BN}(x, v_x, v_y) - f_{MgO}(x, v_x, v_y)$ in 1X2V at $t\omega_{pe} = 3000$. The first four are integrated over the unplotted dimension, the last two are taken at the wall. Accumulation of electrons and ions at the wall for boron nitride is apparent, as well as the deceleration of ions by the potential barrier relative to the magnesium oxide.

where $\mathcal{Q}_{ijk} = m \int v_i v_j v_k f d\mathbf{v}$ is the third moment of the distribution function, p and E are the total fluid pressure and energy, respectively, and π_{ik} is the viscous stress tensor. Heat flux is computed by calculating the other quantities and solving for q_k from Eq. 11. There is significant variation in the heat flux between the different cases. In the classical and high affinity cases, the heat flux remains positive through the sheath

into the wall. Contrarily, heat flux is negative near the wall for the low affinity case. To better understand the reasons behind this somewhat unintuitive result, Fig. 11 plots each of the terms in Eq. 10 and shows how they compare for the three cases inside the sheath region. For the low affinity case, the pressure and energy term increases past the total energy flux density term close to the wall, driving the heat flux negative.

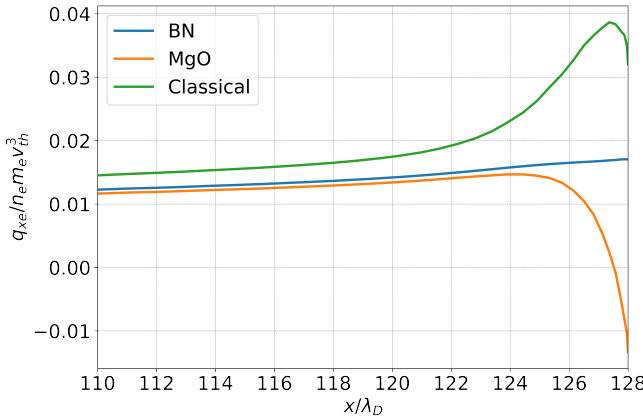


FIG. 10. Comparison of steady-state heat fluxes in and near the sheath region. These quantities are scaled to the density as it decreases into the sheath, not the initial density. Boron nitride and the classical sheath remain positive within the sheath, while magnesium oxide dips negative near the wall.

The reason for this lies in the imbalance of the distribution function. Depletion of the distribution function in the negative direction results in a positive drift speed. However, because the tail of the distribution is in a high-reflection region, the balance of the distribution shifts towards the high-energy tail, causing the average spread (analogous to temperature) to be greater in the negative direction than it is in the positive direction where the distribution is smooth and Maxwellian. Based on Eq. 11, this results in a negative q_{xe} .

V. CONCLUSION

A continuum kinetic framework for simulating electron emission from a dielectric boundary is demonstrated with discussion on properly accounting for source and collision terms and a physical model of the plasma-material interaction derived from first-principles quantum mechanics. The ways in which the material properties of a surface can impact the evolution of the sheath when accounting for electron reflection with this quantum mechanical model are then presented for two different sets of parameters spanning regimes with low and high electron flux gain.

Different materials can significantly impact the electron flux gain in the system, which can drastically change the fundamental sheath potential and density structures, while also greatly affecting the distribution of electrons and energy fluxes experienced at the boundary.

ACKNOWLEDGMENTS

The work presented here was supported by the U.S. Department of Energy ARPA-E BETHE program under Grant No. DE-AR0001263. The authors acknowledge Advanced Research Computing at Virginia Tech for supplying computational resources and support for this work.

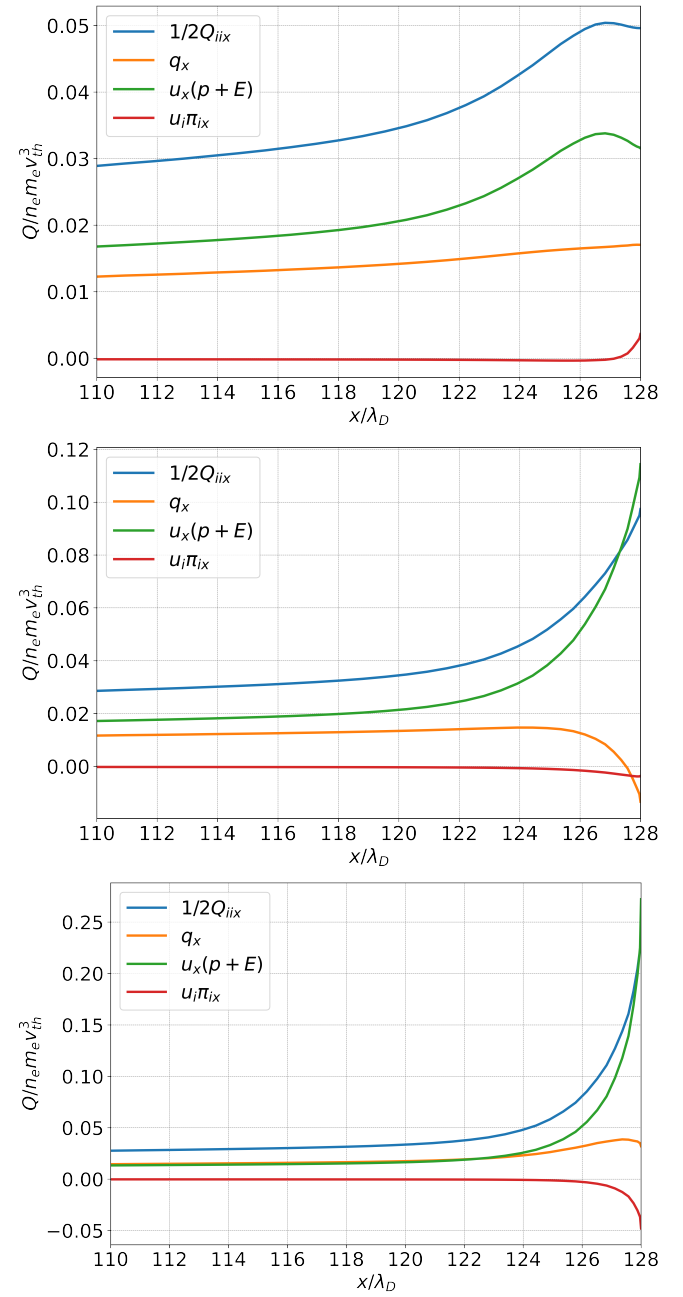


FIG. 11. Plot of the four energy flux density terms in the sheath for boron nitride (top), magnesium oxide (middle), and the classical sheath (bottom). The energy and pressure contribution being greater than the third moment of the distribution moment close to the wall in the magnesium oxide results in the negative heat flux.

¹I. Langmuir, “The effect of space charge and initial velocities on the potential distribution and thermionic current between parallel plane electrodes,” *Phys. Rev.* **21**, 419–435 (1923).

²K. U. Riemann, “The bohm criterion and sheath formation,” *Journal of Physics D: Applied Physics* **24**, 493–518 (1991).

³S. Robertson, “Sheaths in laboratory and space plasmas,” *Plasma Phys. Control. Fusion* **55**, 93001 (2013).

⁴D. Bohm, *The Characteristics of Electrical Discharges in Magnetic Fields* (MacGraw-Hill, New York, 1949).

⁵X.-Z. Tang and Z. Guo, “Critical role of electron heat flux on bohm crite-

rion," (2016), <https://doi.org/10.1063/1.4971808>.

⁶Y. Li, B. Srinivasan, Y. Zhang, and X.-Z. Tang, "Bohm criterion of plasma sheaths away from asymptotic limit," (2022), arXiv:2201.11191 [physics.plasm-ph].

⁷P. Cagas, A. Hakim, J. Juno, and B. Srinivasan, "Continuum kinetic and multi-fluid simulations of classical sheaths," *Physics of Plasmas* **24**, 022118 (2017), <https://doi.org/10.1063/1.4976544>.

⁸M. D. Campanell, "Negative plasma potential relative to electron-emitting surfaces," *Phys. Rev. E* **88**, 033103 (2013).

⁹M. D. Campanell and M. V. Umansky, "Strongly emitting surfaces unable to float below plasma potential," *Phys. Rev. Lett.* **116**, 085003 (2016).

¹⁰J. P. Sheehan, I. D. Kaganovich, H. Wang, D. Sydorenko, Y. Raitse, and N. Hershkowitz, "Effects of emitted electron temperature on the plasma sheath," *Physics of Plasmas* **21**, 063502 (2014), <https://doi.org/10.1063/1.4882260>.

¹¹K. Jensen, *Introduction to the Physics of Electron Emission* (John Wiley & Sons, Inc, New Jersey, 2018) pp. 155–161.

¹²M. A. Furman and M. T. F. Pivi, "Probabilistic model for the simulation of secondary electron emission," *Phys. Rev. ST Accel. Beams* **5**, 124404 (2002).

¹³F. X. Bronold and H. Fehske, "Absorption of an electron by a dielectric wall," *Physical Review Letters* **115** (2015), 10.1103/physrevlett.115.225001.

¹⁴J. P. Dougherty, "Model Fokker-Planck Equation for a Plasma and Its Solution," *Physics of Fluids* **7**, 1788–1799 (1964).

¹⁵B. Cockburn and C.-W. Shu, "Runge–kutta discontinuous galerkin methods for convection-dominated problems," *Journal of Scientific Computing* **16**, 173–261 (2001).

¹⁶A. H. Hakim, G. W. Hammett, and E. L. Shi, "On discontinuous galerkin discretizations of second-order derivatives," (2014), arXiv:1405.5907 [physics.comp-ph].

¹⁷J. Juno, A. Hakim, J. TenBarge, E. Shi, and W. Dorland, "Discontinuous galerkin algorithms for fully kinetic plasmas," *Journal of Computational Physics* **353**, 110–147 (2018).

¹⁸J. Juno, "A deep dive into the distribution function: Understanding phase space dynamics with continuum vlasov-maxwell simulations," (2020), arXiv:2005.13539 [physics.plasm-ph].

¹⁹A. Hakim, M. Francisquez, J. Juno, and G. W. Hammett, "Conservative discontinuous galerkin schemes for nonlinear dougherty–fokker–planck collision operators," *Journal of Plasma Physics* **86**, 905860403 (2020).

²⁰P. Cagas, A. Hakim, and B. Srinivasan, "Plasma-material boundary conditions for discontinuous galerkin continuum-kinetic simulations, with a focus on secondary electron emission," *Journal of Computational Physics* **406**, 109215 (2020).

²¹S. Rumyantsev, M. Levinshtein, A. Jackson, S. Mohammad, G. Harris, M. Spencer, and M. Shur, *Properties of Advanced Semiconductor Materials GaN, AlN, InN, BN, SiC, SiGe* (John Wiley & Sons, Inc., New York, 2001) pp. 67–92.

²²Y.-N. Xu and W. Y. Ching, "Calculation of ground-state and optical properties of boron nitrides in the hexagonal, cubic, and wurtzite structures," *Phys. Rev. B* **44**, 7787–7798 (1991).

²³P. Cagas, "Continuum kinetic simulations of plasma sheaths and instabilities," (2018), arXiv:1809.06368 [physics.plasm-ph].

²⁴P. Cagas, A. Hakim, and B. Srinivasan, "Plasma-material boundary conditions for discontinuous galerkin continuum-kinetic simulations, with a focus on secondary electron emission," *Journal of Computational Physics* **406**, 109215 (2020).

²⁵S. I. Braginskii, "Transport processes in a plasma," (1965).

²⁶L. Wang, A. H. Hakim, A. Bhattacharjee, and K. Germaschewski, "Comparison of multi-fluid moment models with particle-in-cell simulations of collisionless magnetic reconnection," *Physics of Plasmas* **22**, 012108 (2015).